



Enhanced photocatalytic activity by bulk trapping and spatial separation of charge carriers: A case study of defect and facet mediated TiO₂

Zengxia Pei^{a,b}, Sunxian Weng^b, Ping Liu^{b,*}

^a Department of Physics and Materials Science, City University of Hong Kong, Kowloon, Hong Kong SAR, PR China

^b State Key Laboratory of Photocatalysis on Energy and Environment, Research Institute of Photocatalysis, Fuzhou University, Fuzhou 350002, PR China



ARTICLE INFO

Article history:

Received 19 April 2015

Received in revised form 15 June 2015

Accepted 21 June 2015

Available online 30 June 2015

Keywords:

Defect self-doping

Facet

TiO₂

Water splitting

ABSTRACT

Revealing the interplay between composition and structure of a given photocatalyst allows in-depth understanding of the photocatalytic mechanism and also presents as an effective way to optimise the photocatalytic activity. In this work, by studying the property and performance of defect and facet mediated rutile TiO₂ synthesized via a facile oxidation reaction, we demonstrated that the abundant self-doped defects can not only render visible response to the reduced TiO₂ but also suppress the prompt recombination of the charge carriers through bulk trapping, while the {111}–{110} facet couples can induce the spatial separation of the e–h pairs. A synergistic effect between the defects and the facets was observed in the co-mediated TiO₂, and its performance of hydrogen liberation was enhanced by a factor of 18 under simulated solar light compared with referenced commercial rutile, consequently. The present work sheds new light on how the composition and structure of a material can be finely tuned and work synergistically to achieve a much boosted performance.

© 2015 Elsevier B.V. All rights reserved.

1. Introduction

The interplay between the composition and structure on the properties of a certain material has long been a significant theme of material science. While the components lay the foundation for properties, the structure of the material can always dramatically affect its performance. Conversely, rational design of the two factors is also indispensable for specific applications of a material [1,2]. Recent progress in photocatalytic materials has well witnessed this interrelationship, particularly in TiO₂ based photocatalyst [2,3]. In fact, among various materials that have been developed as photocatalyst, titanium dioxide is one of the most promising and popular stuffs owing to its merits like abundance, nontoxicity and high stability. Despite so, the overall efficiency of TiO₂ is restricted to a great extent by the light absorption limitation due to the intrinsic wide band gap and the spontaneous rapid recombination of photogenerated charge carriers within the semiconductor nature [4,5]. Therefore, further works addressing these two barriers are indeed needed for the widespread practical applications of titania.

In the perspective of composition of TiO₂, Ti³⁺ and/or oxygen vacancy (V_O) self-doping, which is developed with respect to heteroatom (including metal and non-metal atoms) doping, has aroused intense research interest in the past a few years [6–12]. Just resembles that in the heteroatom doping methods, the self-doped defects can also introduce extra electronic states in the forbidden band [6–8]. The concentration of the defects, however, should theoretically be high enough to create a new band that eventually leads to the visible light absorption of the TiO₂ [6,7,10]. Up to now, a series of works [7–12] have reported deliberate introduction of Ti³⁺ and/or V_O defects into the bulk lattice of TiO₂ based on either reduction or oxidation methods, and the resulting materials exhibit good photoactivity and stability under visible light. Nevertheless, in many cases, the performance under UV light, of which the incident light possesses higher energy and is much more efficient for TiO₂, is always neglected. Actually, the visible light absorption does not necessarily lead to higher overall performance as defects are sometimes reported to act as annihilation sites especially in the bulk of TiO₂ [13,14]. For example, Liu et al. [14] reported that their Ti³⁺ self-doped TiO₂ showed negligible activity under both UV and visible light though the sample exhibited broad visible light absorption. Leshuk et al. [15] found that the performance of their hydrogenated black TiO₂ under simulated solar light was deteriorated by the introduction of bulk V_O species. Hence, it is still

* Corresponding author. Fax: +86 591 8377 9239.
E-mail address: liuping@fzu.edu.cn (P. Liu).

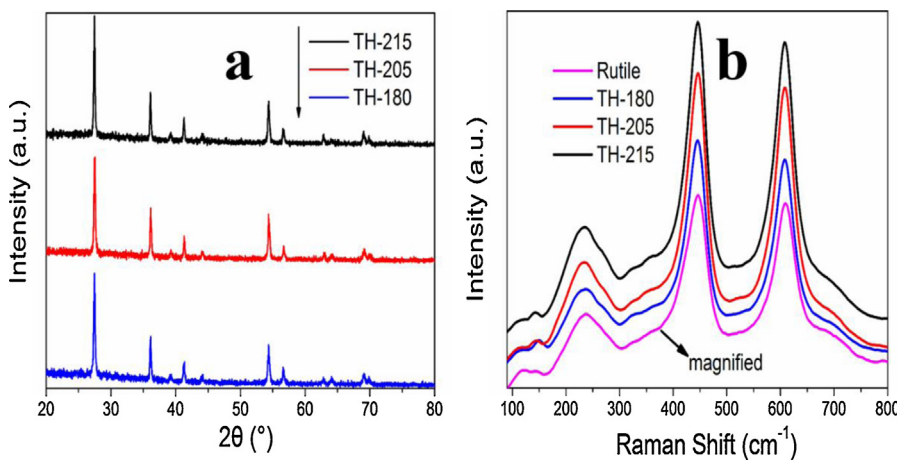


Fig. 1. (a) XRD patterns of the hydrothermal products; (b) Raman spectra of different hydrothermal samples as well as commercial rutile. The spectrum intensity of the referenced rutile is magnified.

necessary to explore other facile and effective strategies to prepare defect-mediated TiO_2 with wide spectral response, high activity as well as good stability.

On the other hand, the fate of the photogenerated charge carriers can be remarkably affected by the architecture of a given photocatalyst [3]. Facet, as a typical micro structure aspect of crystal, has become a research hotspot since distinct atom arrangements and electronic band structures of different facets will influence the transfer pattern of carriers [3,16–20]. Specifically, photoinduced electron and hole can be separately driven to different crystal facets due to the subtle distinction of coupled facets, which thus facilitate the charge separation [16,18]. In this regard, some recent studies have been well conducted in BiVO_4 and anatase TiO_2 systems [18,19]. For rutile, the presence of high energy facets like {111} and {001} can boost the photocatalytic activity, and it is demonstrated that the {111}/{001} and {110} facets of rutile can potentially act as oxidative and reductive sites, respectively [16,21]. Recently, Zuo et al. reported that, in comparison to irregular powder TiO_2 polymorphs, the rutile with {111}–{110} facet couples and bulk Ti^{3+} species showed enhanced performance in hydrogen liberation from water under visible light [10]. Notwithstanding, so far there is still the dearth of the interplay between the defect and facet, their separate and cooperative roles in boosting the photocatalytic activity of TiO_2 , especially under full solar light irradiation.

In the present work, we studied the underlying interplay of the defect and facet by studying the properties of Ti^{3+} self-doped rutile which has explicit facets. A facile oxidation based synthesis process was rationally adopted in hoping of stabilizing Ti^{3+} ions by thermodynamically spontaneous oxidation of Ti^{2+} species from TiH_2 in HCl solution. The products showed a distinct absorption within the whole visible light region as well as some near-infrared light. By simply varying the hydrothermal temperature, Ti^{3+} self-doped rutile with explicit {111} and {110} facets was obtained. It was demonstrated that the abundant defects can not only render visible light response to the reduced TiO_2 but also suppress the prompt recombination of the charge carriers, while the {111}–{110} facet couples can induce the spatial separation of the e–h pairs. A synergistic effect between the defects and the facets was observed and as a result, the performance of hydrogen liberation of the optimised sample was enhanced by a factor of 18 under simulated solar light compared with commercial rutile. The results of this work suggest that the defect composition and the facet structure of a photocatalyst can work cooperatively and be rationally tuned for a much boosted overall activity.

2. Experimental section

2.1. Synthesis of reduced TiO_2

Typically, 400 mg TiH_2 (Alfa Aesar, 325 mesh) powders were dispersed into 25 mL 2 M HCl aqueous solution. The suspension was then transferred into a 50 mL Teflon autoclave and kept at different temperatures (180, 205 and 215 °C) for 12 h. After cooling naturally to room temperature, the precipitate was collected and washed with deionized water for several times until the ionic strength was less than 10 ppm. The clean samples were dried under vacuum overnight. The samples were denoted as TH-x, where x stands for the corresponding hydrothermal temperature.

2.2. Photodeposition of Pt and PbO_2 particles

The selective depositions of Pt and PbO_2 species were carried out to determine the preferred transfer routes of the charge carriers. For Pt deposition, 100 mg of TH-215 sample was dispersed into 100 mL deionized water, and then a certain volume of H_2PtCl_6 was added to ensure the nominal weight ration of Pt– TiO_2 being 3 wt%. The solution was irradiated by full-solar light for 1 h. The powders were then centrifuged and dried at 60 °C in vacuum. This Pt-deposited TiO_2 was then dispersed into 100 mL water again, and 150 mg $\text{Pb}(\text{NO}_3)_2$ was dissolved into the mixture followed by irradiation for another 3 h under solar simulator. The precipitate was then separated out and dried for further analyses.

2.3. Characterization

Crystal structure identification was performed using Bruker D8 X-ray diffractometer (XRD) with Cu K α radiation ($\lambda = 0.15418 \text{ nm}$) operating at 40 kV and 40 mA. Raman scattering measurements were performed with a multichannel modular triple Raman system (Renishaw Co.) with confocal microscopy at room temperature using the 532 nm laser. A 50 \times microscope objective lens was used for focusing the laser beam and collection of the scattered light. Scanning electron microscope (SEM) images were obtained with an FEI Nova NanoSEM 230 field-emission scanning electron microscope. Microstructures and morphologies were investigated using TecnaiG2 F20 S-TWIN (FEI company) Transmission electron microscopy (TEM) with a field emission gun at 200 kV and the accessory Energy dispersive X-ray spectroscopy (EDS) was used to determine the composite elements. Diffuse reflection spectra (DRS) of the samples were recorded on a Varian Cary-500 spectrophotometer and BaSO_4 was used as a reference. X-ray

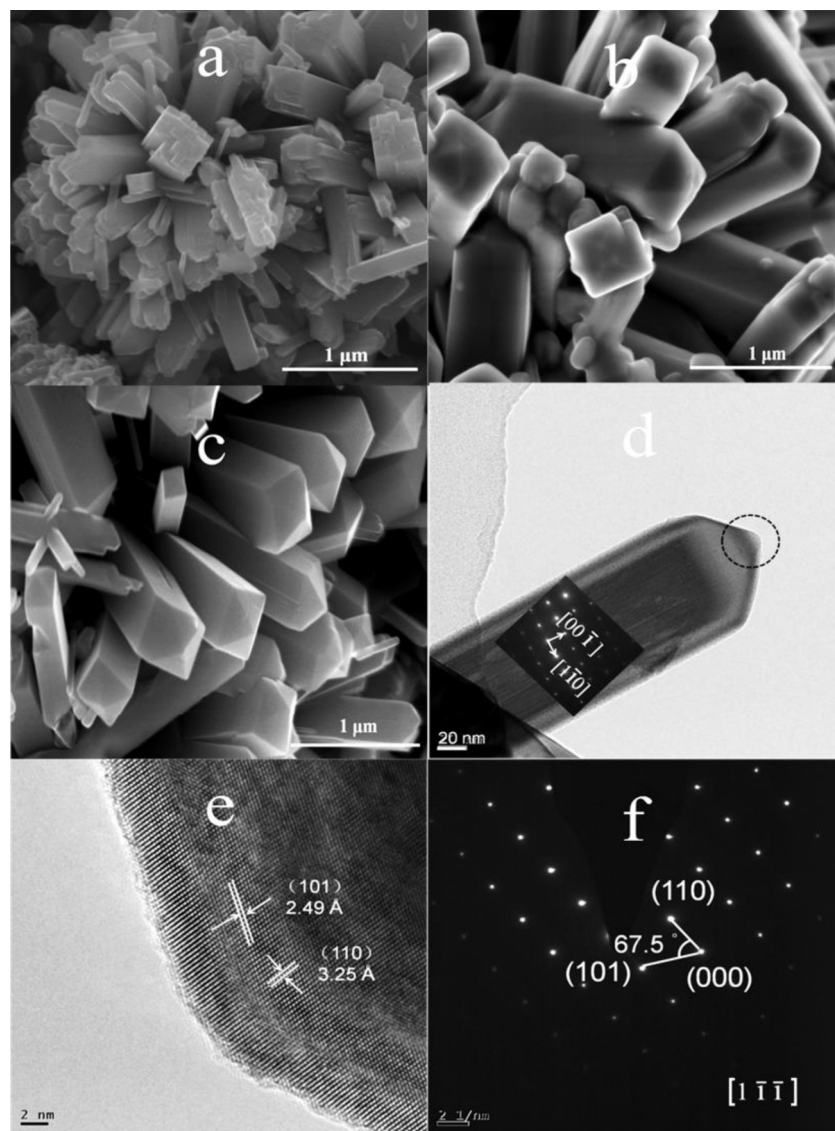


Fig. 2. SEM images of sample (a) TH-180, (b) TH-205, (c) TH-215; (d) TEM image and SAED patterns (Inset) of a single crystal rod of TH-215; HRTEM image (e) and SAED patterns (f) of the top pyramid.

photoelectron spectroscopy (XPS) analysis was conducted on an ESCALAB 250 photoelectron spectroscopy (Thermo Fisher Scientific) at 1.2×10^{-9} mbar using Al K α X-ray beam (1486.6 eV). The XPS spectra are charge corrected to the adventitious C 1 s peak at 284.6 eV. A Bruker model A300 spectrometer was used for detection of the electron-spin resonance (ESR) signals of samples at 77 K. The settings were center field, 3512.48 G; microwave frequency, 9.86 GHz; and power, 6.35 mW. The concentration of Ti $^{3+}$ was determined by a numerical double integration of the ESR spectra and calibrated with Cu $^{2+}$ aqueous solution. The steady state photoluminescence (PL) spectra were obtained using a Varian Cary-Eclipse 500 with an excitation wavelength at 320 nm while the time-resolved PL spectra were got by an Edinburgh FL-FS 920 TCSPC spectrometer. Photoelectrochemical tests were conducted on a ZENNIMUM electrochemical workstation (Zahner, Germany) with a typical three-electrode system. The FTO/TiO_{2-x} film electrodes served as the working electrode. The counter and reference electrodes were Pt plate and Ag/AgCl electrode, respectively. 0.2 M Na₂SO₄ (pH = 6.8) served as electrolyte. The nitrogen adsorption and desorption isotherms were characterized using a Micrometrics ASAP 2020 analyzer.

2.4. Photocatalytic measurements

Photocatalytic H₂ production experiments were conducted in a top-irradiation vessel connected to a glass-enclosed gas circulation system. In a typical run, 0.1 g of sample loaded with 1 wt% Pt was suspended in 100 mL 20% (v/v) methanol aqueous solution under magnetic stirring. After degassing the system for half an hour to remove most of the dissolved oxygen, a 300 W Xe lamp with a 410 nm cut-on filter (PerfectLight Corp.) was applied to execute the photocatalytic reaction. The products were analysed by gas chromatography (Shimadzu GC-8A) equipped with a thermal conductivity detector (TCD). For the first 5-round cycling test, all the H₂ was evacuated off and then another test proceeded, while the samples were sonicated for 5 min before each run in the last 5-round reactions.

3. Results and discussion

The X-ray diffraction patterns in Fig. 1a reveal that all the as-synthesized TiO₂ samples can be identified to be rutile phase. All the peaks can be well indexed to JCPDS card No.01-087-0710, with

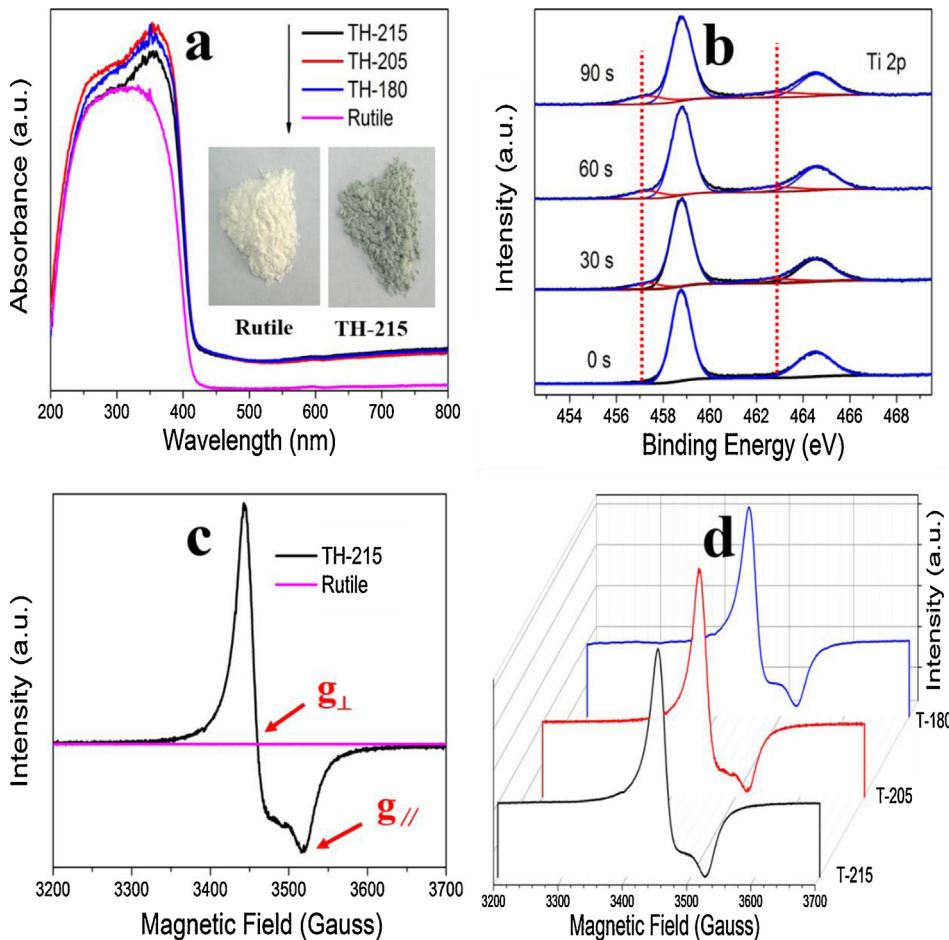


Fig. 3. (a) DRS spectra of the hydrothermal products and commercial rutile, (Inset) Color comparison of the commercial rutile and the TH-215 sample; (b) XPS Ti 2p spectra with different etching time; (c) & (d) ESR spectra of different samples recorded at 77 K in liquid nitrogen.

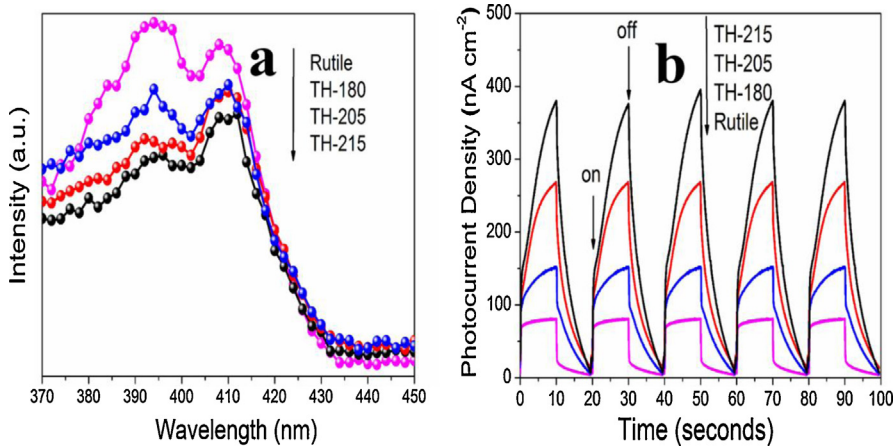


Fig. 4. (a) PL spectra of different samples, with excitation wavelength at 320 nm; (b) Photoelectrical response of different samples under visible light (>410 nm) irradiation.

parameters $a = 4.58 \text{ \AA}$, $c = 2.95 \text{ \AA}$ and the space group $P4_2/\text{mnm}$. No residual TiH_2 is observed, indicating all the TiH_2 has transformed into rutile TiO_2 during the hydrothermal oxidation process. Raman spectra are recorded to further check the surficial structure of the samples. As shown in Fig. 1b, all samples exhibit typical Raman-active modes of rutile at 446 cm^{-1} (E_g) and 611 cm^{-1} (A_{1g}), as well as a multiphonon band at 238 cm^{-1} (E_g) [22]. Considering that Raman spectroscopy is an accurate approach to study the structure changes on the surface of a given material, no distinction in the

defective samples here is an implication that the defects probably locate exclusively in the bulk.

SEM images of the TiO_2 obtained at different hydrothermal temperatures are shown in Fig. 2a–c. After hydrothermal treatment at 180°C , assemblages consisting of individual rods are observed. The single tetragonal crystal has smooth laterals and rough tops, with a length of some $1\text{--}2 \mu\text{m}$ and a nanoscale width (Fig. 2a). It is interesting to note that, as the hydrothermal temperature increases, some ambiguous tetragonal tops take shape while many other ones still

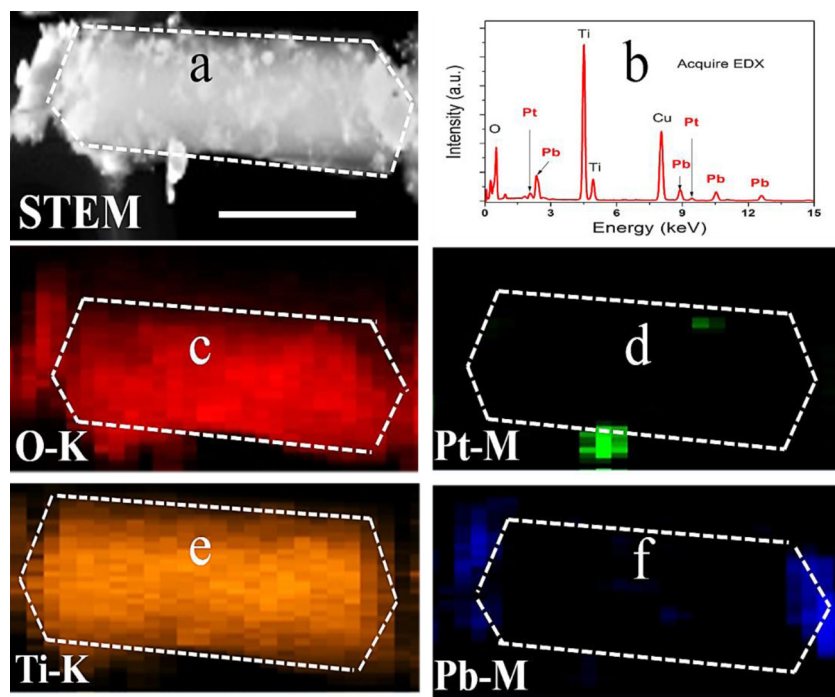


Fig. 5. (a) STEM image of a single rod of TH-215 sample deposited with Pt and PbO_2 , the scale bar in the figure is 500 nm; (b) EDS spectrum measured from the whole field of vision in (a); (c)–(f) elemental mapping reviewing the distribution of different elements in rod crystal.

remain irregular at 205 °C (Fig. 2b). However, when the temperature is further raised to 215 °C, explicit subuliform faces emerge on the topside (Fig. 2c). It is known that the plane with the lowest surface free energy of rutile is {1 1 0} [23]. Also, according to previous investigations, the abundant Cl^- ions in the present reaction system can act as capping agent through adsorption onto the {1 1 0} plane of rutile TiO_2 , leading to an accelerated growth along the [0 0 1] direction [24]. Thus, we deduce that the rod-crystal of rutile consists of lateral {1 1 0} facets, and according to the symmetry of rutile crystal, the tetragonal pyramids take shape at higher temperature can be attributed to {1 1 1} facets. This speculation is verified by TEM analyses. Shown in Fig. 2d is a representative rutile rod-crystal. Inspection on the prismatic plane indicates the lateral faces are assigned to {1 1 0} while the elongation orientation of the crystal is parallel to <001>. High resolution TEM (HRTEM) (Fig. 2e) and selected area electron diffraction (SAED) patterns (Fig. 2f) reviewing the top of the pyramid facet further clearly reveal the crystal lattices and the orientation of the planes. The lattice fringe with d-spacing values of 2.49 Å and 3.25 Å correspond to (101) and (110) planes, respectively. The angle between the two direction is 67.5°, which also confirms the emergence of {1 1 1} facets on the top of the crystal.

The hydrothermal powder product exhibits light bluish-green colour, which is obviously distinct from the commercial white rutile (Fig. 3a, inset). This optical difference is accurately displayed in the UV-vis DRS spectra. As shown in Fig. 3a, the reduced TiO_2 samples have a red-shift of the edge corresponding to the band-to-band transition and a lifted absorption within the whole visible light region, which even extends to near infrared light with respect to commercial rutile. The absorption of visible light is usually reported in defect mediated and heteroatom doped TiO_2 samples [6,7,25,26]. The chlorine doping mechanism seems much more possible as it appears, considering that there are abundant Cl^- ions in the present hydrothermal procedure. However, energy dispersive spectroscopy (EDS) analysis reveals that no chlorine element exists in the reduced TiO_2 (Fig. S1). Survey spectrum of X-ray

photoelectron spectroscopy (Fig. S2a) further confirms this result, in which only Ti and O elements are detected. Therefore, the visible light absorption is reasonably caused by defect self-doping. The O 1 s spectrum is given in Fig. S2b. A strong peak centered at 530.0 eV is attributed to oxygen atoms within the crystal lattice of TiO_2 , while a small shoulder peak at 531.6 eV is generally ascribed to those in surface hydroxyl groups [27]. At the first scan on the surface of the reduced TiO_2 , only Ti^{4+} ions, with characteristic peaks locating at 458.8 eV ($2\text{p}_{3/2}$) and 464.6 eV ($2\text{p}_{1/2}$), are detected (Fig. 3b) [10]. No titanium atoms with low valent state are observed as they are prone to be oxidized by oxygen in the air, and XPS cannot give the information of inner defect due to its limit detection depth. To check the defects inside the bulk, we etched the TH-215 sample with Ar^+ ions for different time. New shoulder peaks at 457.3 ($2\text{p}_{3/2}$) and 463.0 ($2\text{p}_{1/2}$) show up gradually (Fig. 3b) with etching time increasing from 0 to 90 s, both of which correspond to Ti^{3+} ions [10]. It is certainly the case that Ar^+ ions etch will introduce some new Ti^{3+} , but all those in the reduced TiO_2 exhibit more intensive signals in comparison to the referenced commercial rutile after the same etching period (data not shown).

In order to confirm the defects within the bulk of reduced TiO_2 , ESR spectra are then recorded at 77 K. As illustrated in Fig. 3c, the reduced TH-215 sample has an intensive signal in the magnetic field, and g factor values of 1.975 and 1.945 are consistent with perpendicular and parallel ones of the axially symmetric of Ti^{3+} species in rutile, respectively [28]. By contrast, the commercial rutile shows a negligible signal, indicating there is no Ti^{3+} , or its amount is lower than the detection limit under the present condition. These two typical features of Ti^{3+} ions are observed in all the reduced TiO_2 samples as shown in Fig. 3d. Noticeably, the Ti^{3+} ions are exclusively located in the bulk of the reduced TiO_2 , as surface Ti^{3+} ions are sensitive to atmospheric oxygen and will give a paramagnetic signal of O_2^- with g value at approximately 2.02 [7]. Having all the defects located inside the bulk is crucial for the stability of the defective TiO_2 . Actually, the as-synthesized samples did not show noticeable change in the absorbance for more than half a year when stored

in static air. Nevertheless, the sample TH-215 turns white when it is heated at 200 °C in air for 10 h, which firmly suggests that the visible light absorption is caused by defects.

The concentration of the Ti³⁺ defects was also determined by numerical integration of the ESR spectra with Cu²⁺ aqueous solution as calibration reagent. In the typical TH-215 sample, the Ti³⁺ species was calculated to be around 4.3 μmol/g, equivalent to 3.4 × 10¹⁹ spins/mol. This value is quite large and comparable with many ones reported by other researchers [9,28,29]. Also, the Ti³⁺ concentrations in other reduced TH-180 and TH-205 samples are almost the same with that in the TH-215 sample (Fig. 3d), which is in good accordance with their similar light absorption within the visible light region in Fig. 3a. Previous studies [6,7,10] revealed that, with large quantity of Ti³⁺, a continuous vacancy band of electronic states, instead of the localized defect states, can form just below the conduction band edge of TiO₂. This newly introduced electronic band will render positive feedback toward the pristine titania, as we will discuss below.

Fig. 4a presents the steady state photoluminescence spectra of the TiO_{2-x} samples as well as the referenced rutile excited at 320 nm. Two main bands are related to the near band free excitonic emission, both of which show obvious lower intensity in the defective samples. This decline is evidently caused by large quantity Ti³⁺ doping, which can trap photo-induced electrons and suppress the recombination of electron-hole pairs by serving as shallow trapping sites [30,31]. The emission intensity also declines with the increasing percentage of {111} facets on the topside of the rod rutile crystal, and this can be attributed to facilitated charge carriers' separation by the coupling effect between different facets. Earlier studies have demonstrated that the {111} and {110} facets of rutile can act as the oxidative and reductive sites, respectively [9,16,21]. This separation thus accounts for the lowest fluorescence signal of the TH-215 among all reduced TiO₂ samples. Equally important, however, of the grace of the newly formed band is narrowing the band gap of TiO₂ and endows it with visible light activity. The photoelectrical responses of the samples under visible light irradiation (>410 nm) are given in Fig. 4b. Prompt and stable photocurrent is observed for all samples during the on-off cycles of illumination, whereas reduced TiO₂ ones exhibit remarkably increased current density in contrast with the commercial rutile. The TH-215 still shows the highest light-to-electric conversion efficiency, which is consistent with results from the PL test. It is also worth noting that, after illumination, the photocurrent of rutile vanishes almost immediately, yet the reduced TiO₂ samples still show obvious residual current. The slower decay of the photocurrent is an implication that the lifetime of the charge carriers in defective samples is prolonged [25].

To further verify the spatial charge separation caused by the coupled facets in the present system, we conduct the element analyses of TH-215 sample after *in situ* photo-deposition of Pt and PbO₂ species. Generally, once after the separation of the photoinduced charge carriers, the electrons will then transfer to the reductive sites and initiate the reduction reaction, while the holes are prone to gather at the oxidative sites for oxidation reaction [18]. In another word, the different reactions can serve as an evidence to determine the preferred migration orientation of the e-h pairs. Here, we use redox reactions of PtCl₆²⁻ and Pb²⁺ ions as probe reactions and the corresponding reaction processes are depicted by Eqs. (1)–(3):



STEM-EDS analyses in Fig. 5 show that the Pt and PbO₂ are successfully deposited onto the surface of the rod rutile crystal by UV-vis light irradiation, while elemental mappings reveal that Pt

particles locate exclusively on the lateral (110) facet and PbO₂ are mainly deposited onto the pyramidal (111) plane. The separate redox reactions here therefore firmly suggest that the charge carriers are spatially separated, with electron selectively transferring to {110} facets and holes migrating to the {111} ones. It is well studied that, in rutile, the rapid and direct recombination of photo-generated charge carriers makes the span of electron-hole pairs' lifetime extremely short for initiating photocatalytic reactions, which is one of the main reasons for the lower activity of rutile with respect to anatase [32]. Thus, it is an intrinsic way to improve the quantum efficiency of rutile by inhibiting the rapid recombination and prolonging the lifetime of charge carriers.

The photocatalytic activity of the samples is tested by hydrogen liberation from water. 0.1 g of each catalyst loaded with 1 wt% Pt was dispersed into a 100 mL aqueous solution containing methanol 20% (v/v) and irradiated by a 300 W Xe lamp with a 410 nm cut-off filter (see the transmittance spectrum in Fig. S3). Fig. 6a illustrates the time course of H₂ production of different samples under visible light irradiation. The TH-215 sample gives an average H₂ production rate of 138.4 μmol g⁻¹ h⁻¹, which is about 2.5 and 7.2 times higher than TH-205 (55.2 μmol g⁻¹ h⁻¹) and TH-180 (19.4 μmol g⁻¹ h⁻¹), respectively. The corresponding external quantum efficiency (EQE) of the TH-215 sample was measured with a 420 nm band pass filter and the value was calculated to be 1.89%. The surface area of all the samples have also been measured and it is found that the value of TH-215 (4.3 m² g⁻¹) is the smallest among the three reduced TiO₂ samples (7.7 m² g⁻¹ for TH-205 and 11.4 m² g⁻¹ for TH-180) as shown in Fig. S4a. Normally, bigger surface area is expected to achieve higher photocatalytic activity by providing more active sites. The contrary case here firmly indicates the surface area is not the dominant factor in the present system. Hence, the increased photocatalytic activity is reasonably attributed to the coupled facets ({110} and {111}) of TH-215 (Fig. 2c), by which the photogenerated carriers are spontaneously driven to separate. Then we conducted a control experiment by heating the all the reduced TiO₂ samples at 200 °C in air for 10 h (denoted as TH-x-AIR, x stands for the corresponding hydrothermal temperature). As a representative, the TH-215-AIR shows almost no visible light absorption as revealed by DRS spectra (Fig. S5a) and ESR results (Fig. S5b) indicate that Ti³⁺ ions are totally repaired after heating in air. However, the heating process has no influence on the architecture of the sample as the facets of the original TH-215 are well preserved (Fig. S5c). But when executing the water splitting reaction, the heated sample gives drastically dropped activity for H₂ production (only about 5.1 μmol g⁻¹ h⁻¹), which suggests that Ti³⁺ doping is exactly the origin of visible light performance of reduced TiO₂ samples. Moreover, the dependence of H₂ evolution rate of the sample TH-215 on the wavelength of incident light is checked as well (Fig. 6b). A remarkable fall is observed with lengthening the wavelength of the irradiation light, demonstrating the typical light-dependent activity of photocatalytic reactions. Even so, the photocatalyst still exhibits activity under illumination with wavelength larger than 450 nm.

Nevertheless, giving rise to visible light response though, the bulk defects could often deteriorate the overall performance [13–15]. It is therefore highly desired that the extending of visible absorption should not offset the UV activity. Here, we further test the activity of water-splitting of the TH-215 sample under simulated solar light irradiation (approximately 330–1050 nm). Promisingly, the sample still shows an enhanced H₂ production rate of 1.88 mmol g⁻¹ h⁻¹ (Fig. 6c), which is 6.8 times bigger than that of the defect-free TH-215-AIR sample (0.28 mmol g⁻¹ h⁻¹). In addition, this rate is higher than the commercial rutile (~1.4 mmol g⁻¹ h⁻¹), despite the latter has a much larger surface area of 58.8 m² g⁻¹ (Fig. S4b). Therefore, enlarging the surface area

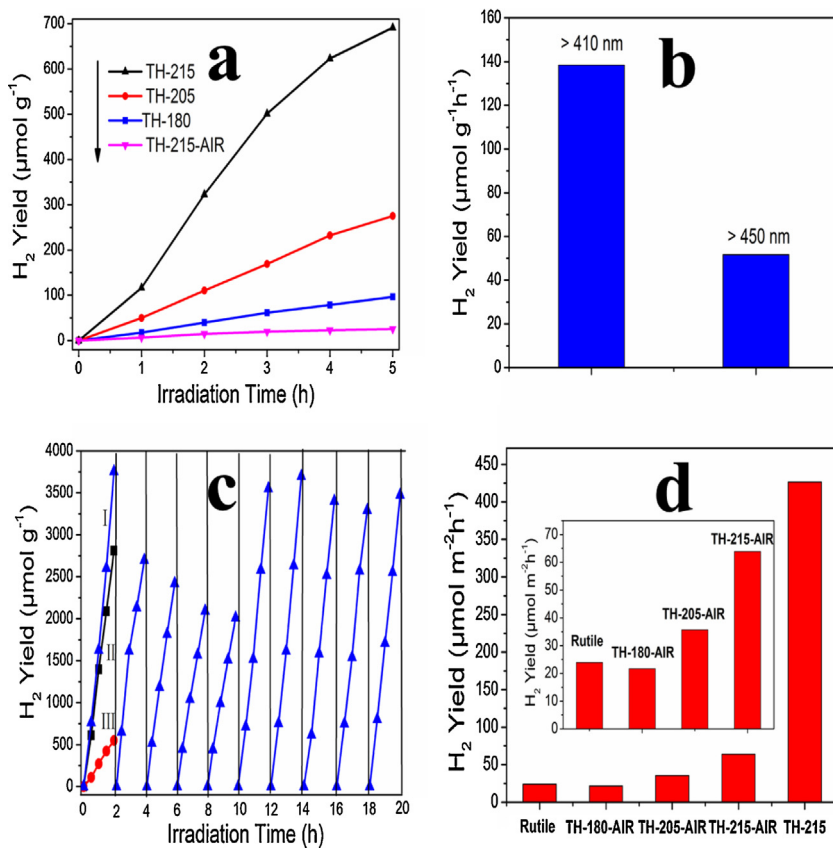


Fig. 6. (a) Time course of H₂ evolution rate of different samples under visible light(>410 nm) irradiation; (b) Wavelength-dependent activity of TH-215 sample under visible light illumination; (c) Cycling tests of TH-215 sample(I) under UV-vis light irradiation, commercial rutile (II) and defect-free TH-215-AIR sample (III) are tested as reference in the first round; (d) H₂ production capability of defect-free samples and the TH-215 sample upon normalization of surface area, (Inset) Magnified histogram of the performance of defect-free samples.

of the reduced TiO₂ may hopefully further improve the activity for H₂ liberation.

It has to be mentioned here that the in the first continuous 5 round cycling tests, the TH-215 presents a gradually decreased performance. We deduce there might be some intermediates from the oxidation of methanol that have blocked the surface of the catalyst [33], even though a specific classification of the intermediates is beyond the scope of the present study. Therefore, in the following, ultrasonic treatment of the sample for 5 min is conducted before each run of another 5 round tests. A steady H₂ production rate is then observed for every cycle. After that, we further perform the ESR analysis of the catalyst and find that the sample displays negligible decrease in the paramagnetic signal (Fig. S6), demonstrating the excellent stability of the defective sample. The H₂-evolution capability of all defect-free samples upon normalization of surface area is given in Fig. 6d. The sample TH-215-AIR still presents peak performance and its hydrogen evolution rate upon normalization of surface area is enhanced by a factor of 2.8 compared with commercial rutile, owing to the charge separation caused by the explicit facets. A dramatic further improvement of the reaction rate with per unit area is bestowed with the presence of Ti³⁺ defects, which further boosts the rate value to about 18 times larger than that of the commercial rutile.

To get an insight into the reason for the enhancement by defects self-doping under full solar light, the samples are analysed by transient fluorescent spectroscopy. As given in Fig. 7, the fluorescence decay kinetics of the TH-215 sample is evidently slower than the defect-free TH-215-AIR sample, indicating the lifetime of the photoinduced charge carrier is prolonged [34]. Since both the two samples preserve {111}–{110} facets, the longer decay time can

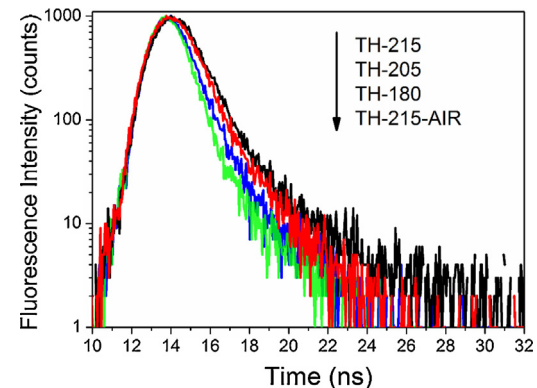


Fig. 7. Time-resolved fluorescent spectra of different samples, with emission band centered around 515 nm.

therefore be reasonably attributed to the abundant bulk defects that had trapped the carriers. Actually, when we check the valence band of the defective TH-215 sample, an obvious tail band that moves toward the vacuum level can be found compared with the defect-free rutile (Fig. S7). This tail band states is usually believed to be caused by large amount of Ti³⁺ induced oxygen vacancies [4,35]. These extended energy states, together with the theoretically formed new bands below the conduction band minimum, can just serve as the trapping sites which cause the prolonged lifetime of carriers and eventually leads to the promoted photocactivity. It is also noteworthy that, in Fig. 7, the fluorescent decay time of TH-215 sample is also slightly longer than those of the TH-180 and TH-

205 samples, indicating that the defect composition and the facet structure work synergistically in the present system, with the bulk trapping and spatial separation of e-h pairs being the main reason for the much boosted performance in water splitting reaction.

4. Conclusions

Summarily, Ti^{3+} self-doped and $\{1\bar{1}0\}$ and/or $\{111\}$ facets exposed rutile TiO_2 samples are synthesized by facile hydrothermal oxidation of TiH_2 in HCl solution at varied temperatures. The *in-situ* generated Ti^{3+} defects can render visible light absorption to the TiO_2 and serve as bulk trapping sites for photogenerated carriers. The $\{1\bar{1}0\}$ – $\{111\}$ couple facets, on the other hand, can facilitate the spatial separation of the e–h pairs. A cooperative effect between the defects and the facets are observed in suppressing the recombination of charge carriers, and thus, the reduced TiO_2 sample with explicit facets shows dramatically improved activity in H_2 liberation from water under both visible light and simulated solar light, as well as excellent stability. It is hoped that the present study may open a new strategy for developing defect and facet mediated photocatalysts and designing other highly efficient and stable photocatalysts driven by solar energy.

Acknowledgements

The work is supported by National Natural Science Foundation of China (No. 21173046, 21473031, 21033003).

Appendix A. Supplementary data

Supplementary data associated with this article can be found, in the online version, at <http://dx.doi.org/10.1016/j.apcatb.2015.06.045>.

References

- [1] H. Tong, S. Ouyang, Y. Bi, N. Umezawa, M. Oshikiri, J. Ye, *Adv. Mater.* 24 (2012) 229–251.
- [2] X. Chen, S.S. Mao, *Chem. Rev.* 107 (2007) 2891–2959.
- [3] G. Liu, J.C. Yu, G.Q. Lu, H.M. Cheng, *Chem. Commun.* 47 (2011) 6763–6783.
- [4] X. Chen, L. Liu, P.Y. Yu, S.S. Mao, *Science* 331 (2011) 746–750.
- [5] M. Liu, X. Qiu, M. Miyauchi, K. Hashimoto, *J. Am. Chem. Soc.* 135 (2013) 10064–10072.
- [6] I. Justicia, P. Ordejon, G. Canto, J.L. Mozos, J. Fraxedas, G.A. Battiston, R. Gerbasi, A. Figueras, *Adv. Mater.* 14 (2002) 1399–1402.
- [7] F. Zuo, L. Wang, T. Wu, Z. Zhang, D. Borchardt, P. Feng, *J. Am. Chem. Soc.* 132 (2010) 11856–11857.
- [8] M. Xing, J. Zhang, F. Chen, B. Tian, *Chem. Commun.* 47 (2011) 4947–4949.
- [9] F. Zuo, K. Bozhilov, R.J. Dillon, L. Wang, P. Smith, X. Zhao, C. Bardeen, P. Feng, *Angew. Chem. Int. Ed.* 51 (2012) 6223–6226.
- [10] X. Liu, S. Gao, H. Xu, Z. Lou, W. Wang, B. Huang, Y. Dai, *Nanoscale* 5 (2013) 1870–1875.
- [11] Z. Wang, C. Yang, T. Lin, H. Yin, P. Chen, D. Wan, F. Xu, F. Huang, J. Lin, X. Xie, M. Jiang, *Energy Environ. Sci.* 6 (2013) 3007–3014.
- [12] X. Chen, L. Liu, F. Huang, *Chem. Soc. Rev.* 44 (2015) 1861–1885.
- [13] M. Kong, Y. Li, X. Chen, T. Tian, P. Fang, F. Zheng, X. Zhao, *J. Am. Chem. Soc.* 133 (2011) 16414–16417.
- [14] M. Liu, X.M. Qiu Miyauchi, K. Hashimoto, *Chem. Mater.* 23 (2011) 5282–5286.
- [15] T. Leshuk, R. Parviz, P. Everett, H. Krishnakumar, R. Varin, F. Gu, *ACS Appl. Mater. Interfaces* 5 (2013) 1892–1895.
- [16] T. Ohno, K. Sarukawa, M. Matsumura, *New J. Chem.* 26 (2002) 1167–1170.
- [17] T. Tachikawa, S. Yamashita, T. Majima, *J. Am. Chem. Soc.* 133 (2011) 7197–7204.
- [18] R. Li, F. Zhang, D. Wang, J. Yang, M. Li, J. Zhu, X. Zhou, H. Han, C. Li, *Nat. Commun.* 4 (2013) 1432.
- [19] N. Roy, Y. Sohn, D. Pradhan, *ACS Nano* 7 (2013) 2532–2540.
- [20] H. Lin, L. Ding, Z. Pei, Y. Zhou, J. Long, W. Deng, X. Wang, *Appl. Catal. B: Environ.* 160–161 (2014) 98–105.
- [21] E. Bae, T. Ohno, *Appl. Catal. B: Environ.* 91 (2009) 634–639.
- [22] O. Frank, M. Zukalova, B. Laskova, J. Kurti, J. Koltai, L. Kavan, *Phys. Chem. Chem. Phys.* 14 (2012) 14567–14572.
- [23] A.L. Linsebigler, G. Lu, J.T. Yates, *Chem. Rev.* 95 (1995) 735–758.
- [24] E. Hosono, S. Fujihara, K. Kakiuchi, H. Imai, *J. Am. Chem. Soc.* 126 (2004) 7790–7791.
- [25] Z. Pei, L. Ding, H. Lin, S. Weng, Z. Zheng, Y. Hou, P. Liu, *J. Mater. Chem. A* 1 (2013) 10099–10102.
- [26] X. Chen, C. Burda, *J. Am. Chem. Soc.* 130 (2008) 5018–5019.
- [27] Z. Pei, L. Ding, W. Feng, S. Weng, P. Liu, *Phys. Chem. Chem. Phys.* 16 (2014) 21876–21881.
- [28] L.R. Grabstanowicz, S. Gao, T. Li, R.M. Rickard, T. Rajh, D. Liu, T. Xu, *Inorg. Chem.* 52 (2013) 3884–3890.
- [29] X. Xin, T. Xu, J. Yin, L. Wang, C. Wang, *Appl. Catal. B: Environ.* 176–177 (2015) 354–362.
- [30] S.W. Chen, J.M. Lee, K.T. Lu, C.W. Pao, J.F. Lee, T.S. Chan, J.M. Chen, *Appl. Phys. Lett.* 97 (2010) 012104.
- [31] D.A. Panayotov, S.P. Burrows, J.R. Morris, *J. Phys. Chem. C* 116 (2012) 4535–4544.
- [32] M. Xu, Y. Gao, E.M. Moreno, M. Kunst, M. Muhler, Y. Wang, H. Idriss, C. Woll, *Phys. Rev. Lett.* 106 (2011) 138302.
- [33] A. Dickinson, D. James, N. Perkins, T. Cassidy, M. Bowker, *J. Mol. Catal. A: Chem.* 146 (1999) 211–221.
- [34] P. Niu, G. Liu, H. Cheng, *J. Phys. Chem. C* 116 (2012) 11013–11018.
- [35] U. Diebold, *Surf. Sci. Rep.* 48 (2003) 53–229.